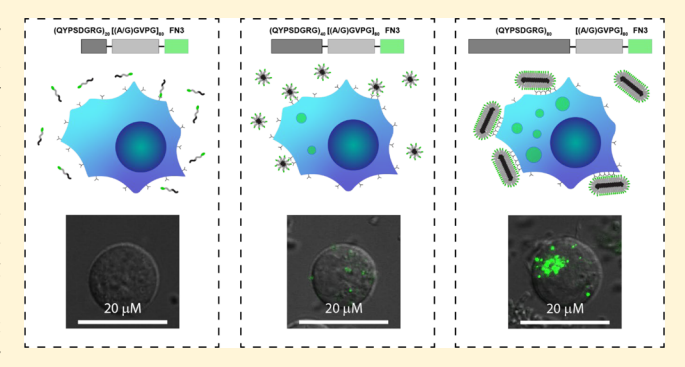
Avidity and Cell Uptake of Integrin-Targeting Polypeptide Micelles is Strongly Shape-Dependent

Michael Dzuricky,^{†©} Sinan Xiong,[†] Patrick Weber,^{†,‡} and Ashutosh Chilkoti*,^{†©}

Supporting Information

Downloaded via DUKE UNIV on December 5, 2019 at 19:18:29 (UTC). See https://pubs.acs.org/sharingguidelines for options on how to legitimately share published articles.

ABSTRACT: We describe a genetically encoded micelle for targeted delivery consisting of a diblock polypeptide with segments derived from repetitive protein motifs inspired by Drosophila melanogaster Rec-1 resilin and human tropoelastin with a C-terminal fusion of an integrin-targeting fibronectin type III domain. By systematically varying the weight fraction of the hydrophilic elastin-like polypeptide (ELP) block and molecular weight of the diblock polypeptide, we designed micelles of different morphologies that modulate the binding avidity of the human wild-type 10th fibronectin domain (Fn3) as a function of shape. We show that wormlike micelles that present the Fn3 domain have a 1000-fold greater avidity for



the $\alpha_s \beta_s$ receptor compared to the monomer ligand and an avidity that is greater than a clinically relevant antibody that is driven by their multivalency. The amplified avidity of these micelles leads to significantly increased cellular internalization, a feature that may have utility for the intracellular delivery of drugs that are loaded into the core of these micelles.

KEYWORDS: Self-assembly, valency, fibronectin type III (Fn3) domain, elastin-like polypeptide, resilin-like polypeptide, micelle

he last few decades have seen an explosion of interest in the development of nanoparticle carriers for drug delivery, much of it for the treatment of solid tumors. Many different types of nanoparticles have been synthesized and evaluated in preclinical models for cancer therapy, including inorganic nanoparticles, 1-4 dendrimers, 5-9 polymer nanoparticles, ¹⁰⁻¹² and self-assembled nanostructures—micelles and polymersomes/liposomes—of polymers ¹³⁻¹⁵ and lipids. 16-18 There are two primary reasons nanoparticles have attracted so much attention from the "nanomedicine" community: First, they can be loaded with a range of small molecules with diverse physicochemical properties, making them nearly universal carriers for small-molecule drugs^{19–21} and imaging agents.^{22–24} Second, appropriately designed nanoparticles can show good colloidal stability in blood and can circulate for extended periods of time^{25–27} in systemic circulation. Because of their potentially long blood circulation, nanoparticles preferentially accumulate in solid tumors due to the enhanced permeability and retention effect, which is a consequence of the aberrant, leaky vasculature in many solid tumors and a poorly developed lymphatic system. 28,29 This approach, via which molecules—and nanoparticles—that have extended blood circulation and that are smaller than a few hundred nanometers in size can escape from the tumor blood vessels and into the tumor, is termed passive targeting.

Passive targeting is enhanced through optimization of the shape, size, and surface charge of nanoparticles. 30-43 Recently, particles with high aspect ratios with high flexibility, referred to as filomicelles, have attracted much research interest due to their long circulation time, high tumor penetration and accumulation, and enhanced active target delivery. 37,43-46 These particles are created via self-assembly or patternmolding, 36 which are convenient to create precise particle shapes but are somewhat incompatible with protein drug cargo or the presentation of protein-targeting ligands, as the conditions employed for their synthesis may denature proteins.

Passive targeting is a useful approach for locoregional targeting of solid tumors, but it does not directly target tumor cells, which are the ultimate destination of the drug or imaging agent. The rationale for creating targeted nanoparticles for cancer therapy or imaging stems from the fact that many tumors have surface proteins that are either overexpressed or-in a few instances-are uniquely expressed on the surface of tumor cells compared to normal, healthy cells. Homing the nanoparticle to tumor cells by decorating it with a ligand specific to a tumor-selective or tumor-specific marker—once the carrier has accumulated to a high enough concentration in the local environment of the tumor—can provide a second stage of tumor-cell-specific targeting.

A common approach to synthesize targeted nanoparticles is to functionalize the surface of the nanoparticle with a peptide or protein by covalent conjugation. This approach however

Received: May 22, 2019 Revised: July 30, 2019 Published: August 7, 2019

Department of Biomedical Engineering, Duke University, Durham, North Carolina 27708, United States

^{*}Swiss Nanoscience Institute, University of Basel, Basel 4056, Switzerland

Table 1. RLP-ELP Diblock Polypeptide Sequence and Molecular Parameters

protein	sequence	MW (kDa)	hydrophilic wt %
RLP ₂₀ -ELP ₈₀ -Fn3	$G-(QYPSDGRG)_{20}-[(A/G)GVPG)]_{80}-Fn3-Y$	57.74	0.70
$RLP_{40}-ELP_{80}$	$G-(QYPSDGRG)_{40}-[(A/G)GVPG)]_{80}-Y$	65.01	0.46
RLP ₄₀ -ELP ₈₀ -Fn3	$G-(QYPSDGRG)_{40}-[(A/G)GVPG)]_{80}-Fn3-Y$	74.96	0.54
$RLP_{40}-ELP_{40}-Fn3$	$G-(QYPSDGRG)_{40}-[(A/G)GVPG)]_{40}-Fn3-Y$	59.57	0.42
RLP ₈₀ -ELP ₈₀	$G-(QYPSDGRG)_{80}-[(A/G)GVPG)]_{80}-Y$	99.46	0.30
$RLP_{80}-ELP_{80}-Fn3$	$G-(QYPSDGRG)_{80}-[(A/G)GVPG)]_{80}-Fn3-Y$	109.4	0.37
$RLP_{80}-ELP_{160}-Fn3$	$G-(QYPSDGRG)_{80}-[(A/G)GVPG)]_{160}-Fn3-Y$	138.9	0.50
Fn3	VSDVPRDLEVVAATPTSLLISWDAPAVTVRYYRITYGETGGNSPVQEFTVPGSKST ATISGLKPGVDYTITVYAVTGRGDSPASSKPISINYRT	9.94	N/A ^a

^aN/A: not applicable.

provides limited control of ligand valency, typically requires an excess of ligand to drive the reaction, and is hence expensive to scale up, and quality control and product validation remains a significant challenge. $^{47-49}$

Our solution to overcome these issues—and one that we and others have pursued—is to leverage recombinant synthesis of an amphiphilic diblock polypeptide fused to a protein ligand that self-assembles into a ligand-decorated micelle—a micelle that presents the targeting protein on the corona of the particle. Motivated by this rationale, in a previous study we reported on a new class of amphiphilic diblock polypeptide with a segment derived from a repetitive hydrophobic peptide motif inspired by Drosophila melanogaster Rec-1 resilintermed resilin-like polypeptide (RLP)—and a second, hydrophilic segment derived from a peptide inspired by human tropoelastin—termed elastin-like polypeptide (ELP)—that self-assemble into spherical and wormlike micelles according to simple design principles. 50,51 These RLP-ELP diblock polypeptides can be easily designed de novo to create thermally stable nanoscale micelles of various sizes and shapes based on the hydrophilic weight percentage of the diblock polypeptide, can be readily manufactured in high yields by recombinant synthesis, and form exceptionally stable micelles with a critical micelle concentration (CMC) of $\leq 0.1 \, \mu M_1^{52}$ features that make them attractive for the design of micelles for the targeted delivery of drugs and imaging agents.

The targeting domain chosen for this study is the 10th, type III domain from human fibronectin (Fn3) that targets the human $\alpha_v\beta_3$ integrin, a receptor that is upregulated in the endothelium of many tumors and is also overexpressed on several tumor cells such as glioblastoma, for renal cell carcinoma, which was an another than the such as glioblastoma, which is also overexpressed on several tumor cells such as glioblastoma, and breast cancer metastases. We chose an Fn3 variant that binds the $\alpha_v\beta_3$ integrin with low affinity $\alpha_v\beta_3$ integrin with low affinity shown that the Fn3 domain can be expressed in Escherichia coli as a fusion to repetitive polypeptides such as ELPs. The low affinity of the parent Fn3 domain is important, as a multivalent presentation could amplify its avidity, which may not be possible with ligands that possess intrinsically high affinity, so that we could test for the effect of self-assembly and multivalency on binding avidity and cellular uptake.

Results and Discussion. Utilizing gene assembly methods that we have previously developed,⁶⁴ we assembled the genes for a set of diblock RLP–ELP diblock polypeptides and cloned them into a modified pET24+ vector for overexpression of the polypeptides in *E. coli*. This set of artificial genes encode RLP–ELPs, wherein the chain length of the core-forming RLP block

is systematically varied while that of the corona-forming ELP block is held constant. A variant of each gene was also synthesized that incorporates the coding sequence for human fibronectin's tenth type III domain at the C-terminus of the diblock polypeptide that binds to the $\alpha_v \beta_3$ integrin. The core block consists of an RLP with the sequence (QYPSDGRG)_n where n=20, 40 or 80, while the corona block consists of an ELP with the repeat sequence ([A/G]PGVG)₈₀. For simplicity, these blocks are hereafter referred to as RLP_n and ELP₈₀, respectively, where n refers to the number of core block repeats. A summary of the amino acid sequence of RLP–ELP diblock polypeptides synthesized in this study and that of the Fn3 domain is in Table 1, and their gene sequences are shown in Table S1.

After assembly of the genes in the expression vector, each vector was transformed into the BL21(DE3) strain of *E. coli* and overexpressed by a previously published protocol. The diblock polypeptides were isolated from the soluble fraction of the cell lysate and purified by inverse transition cycling, a nonchromatographic method, to >95% purity as determined by SDS-PAGE (Figure S1). Yields of all polypeptides were >20 mg $\rm L^{-1}$ of shaker flask culture without any optimization of the expression protocol, similar to typical Fn3 expression and purification schemes that yield 5–20 mg $\rm L^{-1}$.

Each diblock polypeptide was analyzed by dynamic light scattering (DLS) at several temperatures between 4 and 37 °C to determine the thermal stability of the micelles, and to determine their radius of hydration (R_h) . The R_h 's of RLP₂₀-ELP₈₀ and RLP₂₀-ELP₈₀-Fn3 were ~7 nm, indicating that these constructs did not assemble within this temperature range and exist as soluble disordered polypeptides, as their R_h is similar to that of denatured proteins with a similar molecular weight ($R_{\rm h}\sim 8$ nm) and other elastin-like polypeptides of similar size. ^{52,67-69} In contrast, RLP₄₀-ELP₈₀ and RLP₄₀- ELP_{80} -Fn3 self-assembled into micelles with an R_h of 30 and 32 nm, respectively, between 20 and 37 °C (Figures S3 and S4). Likewise, RLP₈₀-ELP₈₀ (112 nm) and RLP₈₀-ELP₈₀-Fn3 (47 nm) formed stable micelles over the same temperature range. Interestingly, the R_h of RLP₈₀-ELP₈₀ is dramatically affected by the presentation of the Fn3 domain on the hydrophilic C-terminal end of the diblock polypeptide. This result makes sense as $RLP_{80}-ELP_{80}$ exists on the edge of the phase boundary that separates spherical and wormlike micelles.⁵² Therefore, it is plausible that the incorporation of a small folded protein could result in a change of shape.⁵² It also appears that the Fn3 domain is not stable at temperatures above 37 °C, as there is a precipitous increase in the $R_{\rm h}$ of RLP₄₀-ELP₈₀-Fn3 between 36 and 40 °C. On the basis of

Table 2. Light Scattering and Surface Plasmon Resonance Data of Block Polypeptides

diblock polypeptide	$R_{\rm g}$ (nm)	$R_{\rm h}~({\rm nm})$	$N_{ m agg}$	$\rho = R_{\rm g}/R_{\rm h}$	shape	$K_{\rm D}$ (nM)
$RLP_{20}-ELP_{80}-Fn3$		6.95			unimer	1190
$RLP_{40}-ELP_{80}-Fn3$	29.3	29.3	201	1.0	spherical	78.9
RLP ₈₀ -ELP ₈₀ -Fn3	39.2	48.7	630	0.8	sphere and wormlike	0.79

this result, samples were maintained on ice prior to flow cytometry and confocal microscopy.

On the basis of our previous results,⁵² we speculated that micelles with an R_h in the 30-40 nm range are likely to be spherical, while micelles with an $R_h > 100$ nm are likely to be cylindrical or wormlike in structure. To deduce the morphology of these particles and to calculate their aggregation number (N_{agg}) , we next carried out static light scattering (SLS) measurements. Increasing the size of the coreforming block from 40 to 80 repeats of (QYPSDGRG) increases the radius of gyration (R_g) from 29 to 39 nm, the R_h from 29 to 49 nm, and the $N_{\rm agg}$ from 201 to 630 chains per micelle (Table 2 and Figure S5). These results suggest that the larger particles have a higher aspect ratio than the smaller particles. Unfortunately, the SLS results were not conclusive, as the form factor $(\rho = R_{\sigma}/R_{\rm h})$ did not change dramatically across particles with putatively different morphologies. Typically, ρ depends on the morphology of the particles with typical values for spheres around 0.7 and increases as the scattering molecule becomes more elongated (i.e., disc-shaped, cylindrical structures).70 Therefore, we next directly visualized the particles with cryo-TEM to confirm their morphology.

Previous studies of ELP-based micelles have demonstrated that the desolvated core of the micelle can be visualized by cryo-TEM, as it has significant differential contrast as compared to the surrounding water, but the corona is far too solvated to be visualized.⁵² Increasing the core-forming RLP block size from 40 to 80 units without an Fn3 domain (Figure 1A,B respectively) shifted the morphology from spherical to wormlike micelles, as reported previously. 52 The core of these micelles increased in diameter (Table S4) from 24 to 59 nm, and the spacing between the particles changed from 27 to 42 nm, indicating the elongation of the corona ELP chain. RLP_n-ELP₈₀-Fn3's behave similarly. Increasing the core size increased the core diameter of the micelles from 27 to 51 nm and the core spacing from 27 to 42 nm (Figure 1C,D respectively). Image analysis suggests a shift in assembly as RLP₄₀-ELP₈₀-Fn3 has >90% of particles with an aspect ratio <2 while RLP₈₀-ELP₈₀-Fn3 has 45% of micelles with an aspect ratio <2 (Figure S12). These results both indicate a shift in morphology from spherical to a mixture of spherical and wormlike micelles. These results also corroborate the DLS and SLS experiments measurements indicating that increasing the core block length elongates the micelle morphology, increasing the density of chains in the corona and maintaining the overall shape of the parent diblock polypeptide. These results also demonstrate the importance of all three complementary techniques to unequivocally determine the assembly state under physiologically relevant conditions. Additional cryo-TEM images can be found in Figure S7.

We next used surface plasmon resonance to characterize the avidity of the RLP_n–ELP₈₀–Fn3 fusions to the ectodomain of human $\alpha_{\nu}\beta_{3}$ integrin. SPR sensorgrams were generated for binding of the Fn3-functionalized RLP–ELP₈₀ diblock polypeptides at concentrations ranging between 2.5 and 10 μ M. Kinetic association ($k_{\rm on}$) and dissociation ($k_{\rm off}$) constants

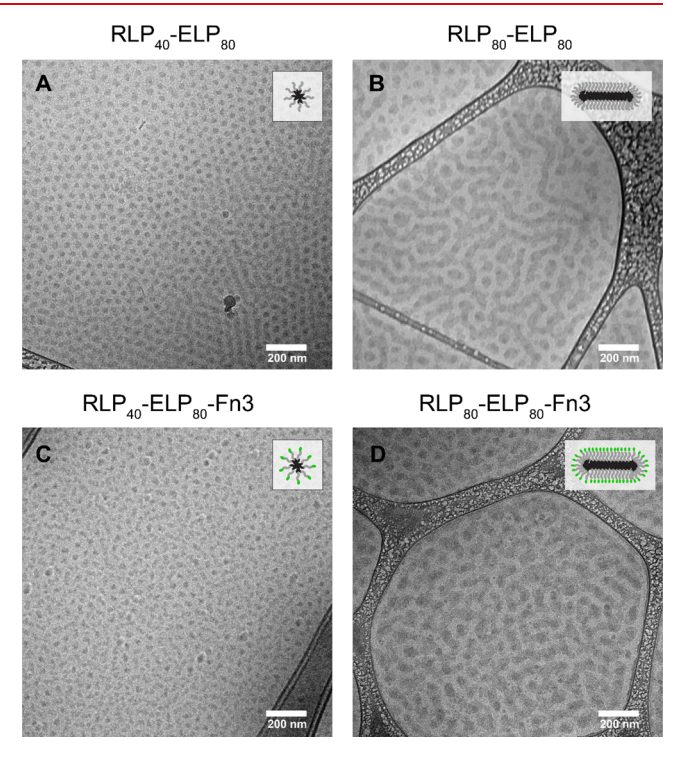


Figure 1. Cryo-TEM Micrographs of RLP $_n$ -ELP $_{80}$ and RLP $_n$ -ELP $_{80}$ -Fn3. (A) Spherical micelles formed by RLP $_{40}$ -ELP $_{80}$. (B) Wormlike micelles formed by RLP $_{80}$ -ELP $_{80}$. (C) Spherical micelles formed by RLP $_{40}$ -ELP $_{80}$ -Fn3. (D) Spherical and wormlike and spherical micelles formed by RLP $_{80}$ -ELP $_{80}$ -Fn3. All scale bars represent 200 nm. All data collected at 15 °C in 150 mM PBS at 10 μ M.

are summarized in Table S3. As the core block size increases, the $k_{\rm on}$ increases in magnitude, and the $k_{\rm off}$ decreases in magnitude, both consistent with the increase in size of the binding unit (unimer or larger diameter micelle).⁷¹ As seen in previous studies, 38,72 Fn3-decorated spherical micelles showed a 10-fold increased avidity for the $\alpha_{\nu}\beta_{3}$ integrin compared to the RLP₂₀-ELP₈₀-Fn3 construct that does not self-assemble and hence only presents a single copy of the Fn3 domain. Interestingly, elongating the particle from a spherical to wormlike geometry can increase the avidity for the integrin by ~1000-fold compared to the monomer ligand, driving avidity into picomolar concentrations (Figure 2). This result is remarkable when one considers the unoptimized nature of the Fn3, which has K_d in the micromolar range for the $\alpha_v \beta_3$ integrin. The effective K_d of the RLP_n-ELP₈₀-Fn3 wormlike micelles is in fact many orders of magnitude lower than that of a clinically relevant therapeutic antibody—LM609—which has a K_d of ~20 nM.⁷³ For context, these binding constants are at the upper threshold of antibodies that are used for targeted cancer therapy, highlighting their clinical relevance.

To assess the intracellular uptake of these particles, we used a cell line stably transfected with the $\alpha_v \beta_3$ integrin. The native cell line, K562, has endogenously low levels of expression of this receptor and therefore serves as the receptor-negative

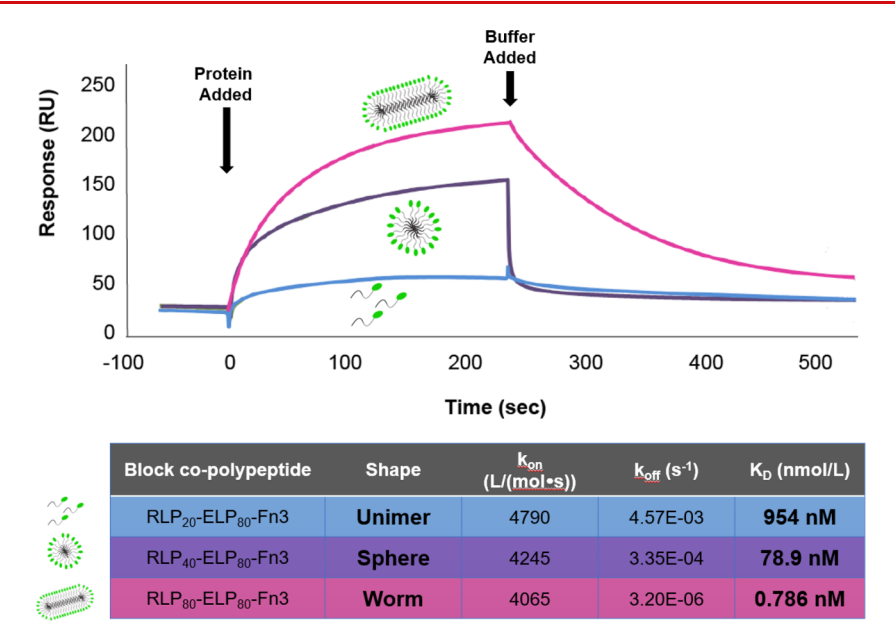


Figure 2. Shape-dependent avidity of RLP_n–ELP–Fn3. Multivalency increases the observed K_D as does increasing the aspect ratio of the micelle. Representative SPR sensorgrams shown on top show a marked decrease in k_{off} between the unimer and spherical and wormlike micelles. In contrast the k_{on} is similar for all constructs of interest. SPR sensorgram data collected in PBS at 10 μM.

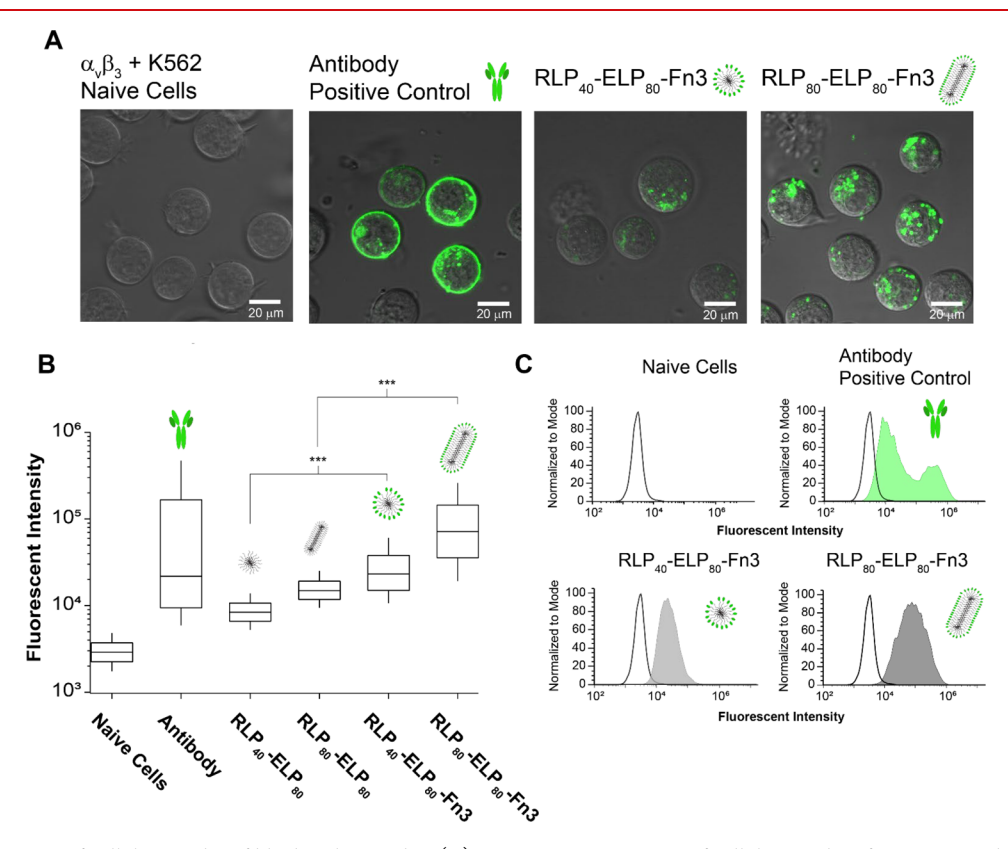


Figure 3. Quantification of cellular uptake of block polypeptides. (A) Representative images of cellular uptake of RLP_n–ELP diblock polypeptides labeled with Alexa488 fluorophore (green) overlaid with DIC images (gray) after 2.5 h of incubation in serum-free minimal media at 10 μ M. Scale bar = 20 μ m. (B) Quantification of cellular uptake by flow cytometry. *** = p < 0.001. Box indicates 25th and 75th percentile and bars indicate 10th and 90th percentile. (C) Flow cytometry data of naïve cells, LM609 antibody, RLP₄₀–ELP₈₀–Fn3 spherical micelles, and RLP₈₀–ELP₈₀–Fn3 wormlike micelles.

control, and the undecorated RLP $_n$ –ELP $_{80}$ micelles serve as ligand-negative controls for each type—size and shape—of micelle. Cells were incubated for 2 h with a 10 μ M solution of various diblock polypeptides at 37 °C, a concentration that is well above the CMC 52 and $K_{\rm d}$ of all micelles. Confocal

microscopy was first used to study the internalization of the diblock polypeptides by the $\alpha_v \beta_3$ integrin transfected cell line. Ligand-negative spherical micelles showed low levels of uptake, while that of ligand-negative wormlike micelles was slightly higher (Figure S8A), consistent with previous observations

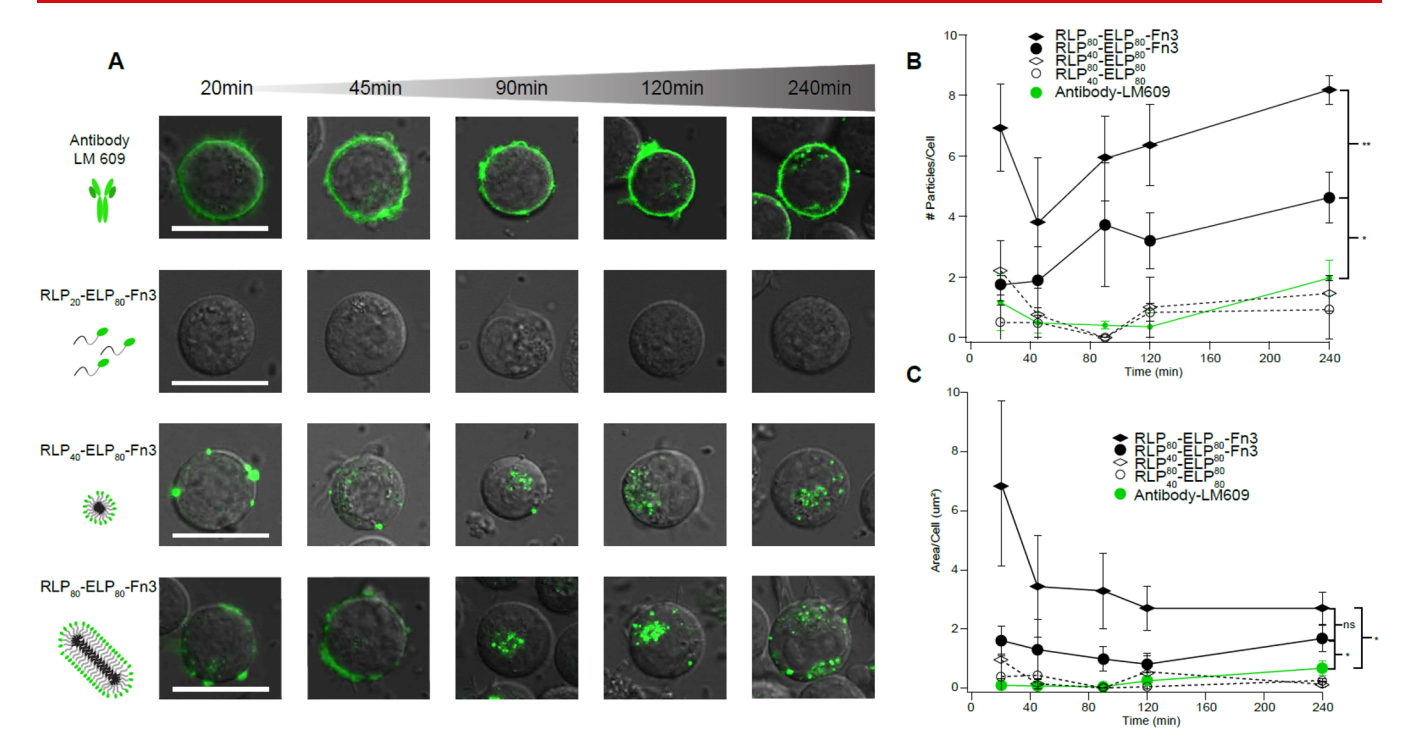


Figure 4. Cellular uptake of block polypeptides over time reveals increased binding and penetration of spherical and wormlike micelles. (A) Representative confocal images of antibody (LM609), $RLP_{20}-ELP_{80}-Fn3$, $RLP_{40}-ELP_{80}-Fn3$, and $RLP_{80}-ELP_{80}-Fn3$ uptake as a function of time. Scale bar = 20 μ m. (B) Quantification of number of intracellular particles over time by image analysis. (C) Quantification of the area of intracellular particles over time by image analysis. * = p < 0.05, ** = p < 0.01, *** = p < 0.001. Error bars indicate standard deviation.

that shape plays a role in controlling nonspecific uptake of nanoparticles. 75,76 However, far more dramatic differences were seen for Fn3-decorated micelles. Compared to the parent spherical micelle which showed a low level of uptake (Figure S8A) that was barely above that of the autofluorescence of the WT-untransfected-cell line, presentation of the Fn3 domain on the RLP_n-ELP₈₀ diblock polypeptide that forms spherical micelles significantly increased its uptake (Figure 3A) as quantified by the number of particles inside the cell membrane (Figure S8B) and the mean fluorescence of the cell (Figure 3B p < 0.001 unpaired Student's t test). The wormlike micelles that are decorated with the Fn3 ligand similarly showed a much greater level of cell uptake compared to the parent wormlike micelles (Figure 3A). In contrast, without overexpression of the $\alpha_{\nu}\beta_{3}$ integrin on K562 cells, there were low levels of internalization and uptake of the spherical and Fn3-decorated micelles, showing that most internalization of ligand-decorated micelles is driven by ligand-receptor engagement (Figure S7).

The LM609 antibody showed a completely different cell uptake than RLP–ELP $_{80}$ –Fn3 micelles. Although it has a high level of fluorescence (Figure 3A), much of the fluorescence was localized at the cell membrane, and there were far lower levels of intracellular fluorescence, especially compared to the Fn3-decorated micelles, indicating that this particular antibody–integrin binding event does not trigger internalization.

Flow cytometry was next used to quantify the cell uptake. Unstained K562 cells had a background cell fluorescence of 2912 \pm 3236 (geometric mean \pm standard deviation) (Figure 3C) which increased to 8686 \pm 8787 when incubated with RLP₄₀–ELP₈₀ spherical micelles and to 24 904 \pm 13 884 for the RLP₈₀–ELP₈₀ indicating that there is a low-level but shapedependent nonspecific uptake of the micelles (p < 0.001,

unpaired Student's t test) (Figure 3B). The positive control, the LM609 antibody, had a statistically significantly higher uptake of 36708 ± 255175 , consistent with its known specificity for the $\alpha_{\nu}\beta_3$ integrin (Figure 3B). A closer look at the flow cytometry data indicates that there is a high-level and low-level receptor expressing cell population, as seen by the two distinct peaks in Figure 3C. Interestingly, spherical micelles formed by RLP₄₀-ELP₈₀-Fn3 and wormlike micelles formed by RLP80-ELP80-Fn3 have higher geometric fluorescent intensity means of 15 539 \pm 286 229 and 71 382 \pm 251 919 that are 2-fold and 3-fold greater than the undecorated controls (Figure 3C). Clearly receptor-mediated endocytosis is shape-dependent, as seen by the significantly higher cell uptake exhibited by the wormlike micelles compared to spherical micelles, that is also consistent with their higher avidity for the integrin. The Fn3-decorated spherical and wormlike micelles also only exhibited a single flow cytometry peak, unlike LM609 that has a bimodal distribution of cell uptake. This result implies that high-valency micelles are not sensitive to the heterogeneity of receptor expression, presumably as long as the receptor expression is above a certain threshold to enable multiple ligands to engage the receptors on the cell surface. High-valency micelles may therefore provide a more robust strategy to target cells with inhomogeneous levels of receptor expression than antibodies. A full description of the flow cytometry data can be found in Table S2.

We next decided to visualize the kinetics of internalization by imaging the cells at 20, 45, 90, 120, and 240 min postincubation (Figure 4). Particle and area analysis of the Alexa488 dye was performed on all cells in the visual field for at least 3 separate images resulting in ~50 individual cells included for each time point. The analysis area was gated to exclude the cell membrane to eliminate noninternalized areas

of fluorescence. Compared to the LM609 antibody that remains largely associated with the cell membrane, with only a few isolated fluorescent puncta within the cell at later points, spherical (RLP₄₀-ELP₈₀-Fn3) and wormlike (RLP₈₀-ELP₈₀-Fn3) micelles are internalized faster, resulting in more particles within the cell at all time points. Using a 3-way ANOVA for time, shape, and decoration state (Fn3±) we observed a main effect of shape, decoration state, and time for both the number of particles and the area which they cover in the cell. Pairwise interactions indicate that there are significant effects of micelle shape on the number of particles per cell between spherical and wormlike micelles (p < 0.01) and spherical micelles and the positive—antibody—control (p < 0.05). There were significant differences in the area these particles occupied in the cell between spherical micelles and the antibody control over time (p < 0.05) and wormlike micelles and the antibody control (p < 0.05) over time. There was not a significant difference in particle area between spherical and wormlike micelles over time. The overall percentage of the cell population that contained the fluorescent signal was evaluated but did not produce a significant effect over time. The only significant effects of this ANOVA analysis were pairwise effects of micelle shape over time (p < 0.001) and decoration state over time (p < 0.01) (Tables S5–S7). In summary these data show that there is (i) a statistically significant increase in cellular uptake with respect to particle morphology and (ii) a statistically significant increase in cellular uptake by micelles that present an integrin-binding Fn3 domain.

Discussion and Conclusions. Our results clearly show that RLP_n-ELP₈₀ diblock polypeptides are a robust platform for the multivalent display of Fn3 domains via self-assembly of the polypeptides into micelles. The morphology of the parent micelles-spherical versus wormlike-can be tuned by modulating the block ratios and the molecular weight of the core. Decreasing the hydrophilic weight fraction from ~0.7 to ~0.46 to ~0.30 changes the morphology from unimers to spherical micelles to wormlike micelles, respectively. Importantly, the gene-level fusion of the Fn3 domain that targets the $\alpha_{v}\beta_{3}$ integrin at the hydrophilic, C-terminal end of the diblock RLP-ELP polypeptide does not abrogate self-assembly and enables the high-density presentation of an Fn3 domain on the corona of the micelles. Fn3 presentation does, however, have an impact on morphology, as the parent micelle, RLP80-ELP₈₀, that exists on the phase boundary between spherical and wormlike micelles, converts to a mixture of spherical and wormlike micelles upon presentation of the Fn3 domain on the corona of the diblock polypeptide.

Cell uptake studies of Fn3-presenting RLP-ELP diblock polypeptides with an $\alpha_y \beta_3$ overexpressing cell line yielded four notable results: First, compared to the parent—ligand-negative micelles—that in the best case—a wormlike micelle—has 3fold greater cell uptake at 2 h, demonstrates that multivalency can greatly enhance the targeting potency of a ligand simply by virtue of the avidity effect. Second, compared to an RLP_n-ELP-Fn3 fusion that does not self-assemble into a micelle and hence only presents a single copy of the Fn3 domain that target the $\alpha_{\nu}\beta_{3}$ integrin, we found that multivalent spherical and wormlike micelles have a higher avidity and greater cellular uptake, showing the importance of multivalency in amplifying the avidity of a ligand by presentation of multiple copies on a nanoscale scaffold. Third, we observed a dramatic difference in cell uptake as a function micelle morphology, where Fn3decorated wormlike micelles showed a 5-fold increase in cell

uptake compared to spherical micelles. Fourth, we believe that morphology is more important than size, as wormlike micelles with the same hydrophilic weight fraction as $\rm RLP_{80}-\rm ELP_{80}-\rm Fn3$, but that are smaller in size, exhibit higher levels of cell uptake than a spherical micelle of comparable size (RLP_{40}-ELP_{80}-\rm Fn3). Likewise, spherical particles of a similar size as compared to the wormlike micelle of $\rm RLP_{80}-\rm ELP_{80}-\rm Fn3$ exhibit very low levels of uptake (Figures S10 and S11). These data indicate that the elongated shape and flexibility of the wormlike micelles increased the number of accessible Fn3 ligands available to bind the receptor. Fifth, the avidity and cell uptake of the best performing wormlike micelles is greater than that of a therapeutically relevant antibody that targets the same receptor.

This class of self-assembling RLP-ELP diblock polypeptides provides an exceptionally robust and versatile system for the synthesis of recombinant micelles for delivery of drugs and imaging agents for the following reasons, compared to other ELP-based nanostructures: First, RLP-ELP diblock polypeptides, unlike ELP diblock polypeptides, 82 follow canonical rules of polymer self-assembly via genetic encoded sequences, which make it easier to program their morphology de novo for specific applications. Second, these micelles have significantly greater thermodynamic stability than ELP micelles, as they have CMCs in the $\leq 0.1 \,\mu\text{M}$ range, compared to the 5–10 μ M CMC of ELP micelles. Third, these micelles enable presentation of an Fn3 domain on their corona, which is an attractive choice as a targeting ligand, as the Fn3 scaffold is an enormously mutable targeting scaffold and allows variants to be discovered by library screening approaches against diverse targets. Fourth, we note that these targeted micelles can be loaded with drug simply by conjugation of small-molecule drugs into the core-forming, hydrophobic domain, in a manner similar to our previous ELP micelles. Finally, their manufacturing—and hence clinical translation—can leverage the bacterial fermentation and downstream purification capabilities of the biopharmaceutical industry. In future work, we plan to introduce small-molecule drugs and imaging payloads into the core of these micelles for chemotherapy and functional imaging of tumors.

Materials and Methods. Materials. Oligonucleotides encoding ELP sequences were purchased from Integrated DNA Technologies (Coralville, IA). Competent Escherichia coli BL21 expression cells were purchased from New England Biotech (Ipswich, MA). Terrific Broth (TB) dry powder growth media was procured from MO BIO Laboratories (Carlsbad, CA). Kanamycin sulfate was purchased from EMD Millipore (Billerica, MA), and isopropyl- β -D thiogalactoside (IPTG) was purchased from Gold Biotechnology (St. Louis, MO). Calbiochem phosphate buffered saline (PBS) tablets (10 mM phosphate buffer, 140 mM NaCl, 3 mM KCl, pH 7.4 at 25 °C) and low-retention 0.45 µm Millex-HV filters were procured from EMD Millipore (Billerica, MA). SimplyBlue Stain and NHS Ester Alexa Fluor 488 dye were purchased from Thermo Fisher Scientific (Waltham, MA). Mini-PROTEAN TGX stain-free precast gels were purchased from Bio-Rad Laboratories (Hercules, CA).

Gene Assembly. Plasmid genes were available from previous studies for RLP₂₀, RLP₂₀–ELP₈₀, RLP₄₀–ELP₈₀, RLP₈₀–ELP₈₀, RLP₁₀₀–ELP₈₀, and an Fn3 domain that binds the $\alpha_{\rm v}\beta_3$ integrin. S2,60 This gene was then subsequently fused with the gene that encodes the Fn3 domain. Similarly, genes encoding RLP₂₀–ELP₈₀, RLP₄₀–ELP₈₀, and RLP₈₀–ELP₈₀

were cloned to the N-terminus of an Fn3 with the same directional ligation method. 64 After successful confirmation of gene assembly by Sanger fluorescent DNA sequencing, the plasmids harboring each construct were isolated and transformed into the BL21(DE3) expression strain of *E. coli*. Aliquots of the cell stocks were stored at -80 °C until further use.

Expression and Purification. Each block polypeptide was expressed in BL21(DE3) E. coli using a previously published hyperexpression protocol. Bacterial cultures (5 mL) were grown overnight from frozen glycerol stocks and used to inoculate 1 L flasks of TB Dry, supplemented with 45 μ g mL⁻¹ kanamycin. The flasks were then incubated at 37 °C for 24 h and 190 rpm. Each construct was purified using inverse transition cycling (ITC).65 Briefly, the cell suspension was centrifuged at 3000 rpm for 10 min at 4 °C; the cell pellet was then resuspended in PBS and then lysed by sonication on ice for 2 min (10 s on, 40 s off) (Misonix S-4000; Farmingdale, NY). Polyethyleneimine (PEI) 0.7% w/v was added to the lysate to precipitate nucleic acid contaminants. The supernatant was then subjected to multiple rounds of ITC as follows: the solution was kept on ice, and 3 M NaCl was added to isothermally trigger the phase transition of the RLP-ELP diblock polypeptide. The coacervate was then centrifuged for 20 min at 14 000g and 30 °C; the supernatant was decanted and discarded, and the pellet was resuspended in phosphate buffer. The dissolved product was cooled to 4 °C and then centrifuged for 10 min at 15 000g and 4 °C to remove any insoluble contaminants. To remove excess salt from purified protein solutions, the samples were dialyzed against ddH₂O at 4 °C for at least 24 h using SpectrumTM Laboratories Spectra/PorTM 2 12-14 Standard RC dry dialysis kits (Fisher Scientific, Waltham, MA). The proteins were then lyophilized and stored at -20 °C. Purity of the block polypeptides was assessed by SDS-PAGE gel with SimplyBlue staining (Figure S1).

Temperature-Dependent Dynamic Light Scattering (DLS). Temperature-programmed DLS was carried out using a Dynapro plate reader (Wyatt Technology; Santa Barbara, CA) with samples filtered through 0.45 μ m Millex-GV filters. Data were collected at increments of 1 °C, and the DLS data were analyzed by fitting the autocorrelation function with a Rayleigh-sphere cumulant fit model to determine $R_{\rm h}$.

Static Light Scattering (SLS). Static and dynamic light scattering measurements (SLS/DLS) were performed on an ALV/CGS-3 goniometer system (Langen, Germany). Samples for the ALV/CGS-3 goniometer system were prepared at a concentration of 10 μ M in PBS and filtered through 0.45 μ m Millex-GV filters into a 10 mm diameter disposable borosilicate glass tube (Fischer). Simultaneous SLS and DLS measurements were carried out at 15 °C for angles between 30° and 150° at 5° increments, with each angle consisting of 3 runs for 15 s. SLS experiments were only carried out for the block polypeptides that self-assemble into micelles, as the molecular weights of polypeptide unimers were already known from their amino acid sequence, and the R_g of a single chain is below the detection limit of the SLS instrument. The differential refractive index (dn/dc) was determined by measuring the refractive index at different concentrations using an Abbemat 500 refractometer (Anton Paar, Graz, Austria). DLS data were analyzed by fitting the autocorrelation function with a cumulant fit, using the built-in ALV software. The R_h reported is an estimation of the R_h at zero angle from a

multiangle extrapolation. SLS data were analyzed by partial Zimm plots using ALVSTAT software to determine the $R_{\rm g}$ and molecular weight of the micelles (MW).

Cryo-TEM. Cryo-TEM experiments were performed at Duke University's Shared Materials Instrumentation Facility (Durham, NC). Lacey holey carbon grids (Ted Pella, Redding, CA) were glow discharged in a PELCO EasiGlow cleaning system (Ted Pella, Redding, CA). A 3 μ L drop (10 μ M RLP_n–ELP₈₀) was deposited onto the grid, blotted for 3 s with an offset of –3 mm, and vitrified in liquid ethane using the Vitrobot Mark III (FEI, Eindhoven, Netherlands). Prior to vitrification, the sample chamber was maintained at 15 °C and 100% relative humidity to prevent sample evaporation. Grids were transferred to a Gatan 626 cryoholder (Gatan, Pleasanton, CA) and imaged with an FEI Tecnai G2 Twin TEM instrument (FEI, Eindhoven, Netherlands), operating at 80 keV. Feature sizes and spacing distances were measured in ImageJ by manual measurement of at least 25 particles.

Surface Plasmon Resonance (SPR) Spectrometry. The surface plasmon resonance experiments were performed using a Biacore T200 instrument. Purified human $\alpha_y \beta_3$ integrin (Chemicon, Temecula, CA) was immobilized on research grade CM5 sensor chips using an amine coupling kit (BIAcore, Piscataway, NJ). The integrin was diluted in 10 mM sodium acetate buffer (pH 4.5) for conjugation with a surface density of approximately 600 resonance units (RU). The measurements of binding events were performed using block copolypeptide concentrations ranging between 2.5 and 10 μ M. The block polypeptides were diluted in HBS-P buffer (10 mM HEPES, 150 mM NaCl, 0.005% Triton-X, pH 7.4) supplemented with 2 mM CaCl₂ and injected into the flow cells at a flow rate of 30 μ L min⁻¹ for 4 min. The complex was allowed for dissociation for 10 min. The surface was regenerated with 10 mM glycine-HCl (pH 2.5) at a flow rate of 30 μ L min⁻¹ for 45 s, followed by 10 mM glycine–HCl (pH 2.0) at a flow rate of 30 μ L min⁻¹ for 30 s. The surface was regenerated using 10 mM glycine-HCl (pH 2.0). Kinetic modeling and simulations were performed using BIAevaluation software with the heterogeneous ligand model for selfassembled proteins and with a 1:1 ligand model for the unimeric protein (RLP₂₀-ELP₈₀-Fn3). The equilibrium binding constants (K_{D1} and K_{D2}) for each experiment were calculated by dividing the kinetic dissociation rate (k_{off}) by the association rate (k_{on}) , from which the mean $K_{D1/2}$ was derived (Table S3). All SPR measurements were carried out at 25 °C. The SPR measurements were carried out using polypeptide concentrations ranging between 2.5 and 10 µM. Goodness-offit was evaluated by analyzing residual plots and the residual sum of squares.

Flow Cytometry. Approximately 1×10^6 cells were harvested from either K562 or K562+ $\alpha_{\rm v}\beta_3$ cell lines and resuspended into 1 mL of serum-free medium containing 10 $\mu{\rm M}$ of the various Fn3-decorated and control block polypeptides. LM609 antibody was also resuspended at 10 $\mu{\rm M}$ in serum-free medium. Micelles were prepared from a mixture of ~10% Alexa 488 dye-labeled RLP—ELP diblock polypeptides and 90% unlabeled polypeptides on a molar basis. The cells were incubated at 37 °C with the labeled micelles for a specified time and then rinsed with 1 mL of Hank's buffered saline solution (HBSS), collected by centrifugation at 500 RCF for 5 min at 20 °C, and resuspended in HBSS + 1% BSA. Cells were maintained on ice until they were analyzed by flow cytometry (BD Accuri C5). The cell fluorescence intensity of

Alexa 488 (Green) was quantified after gating to remove cellular debris on unstained control samples.

Confocal Microscopy. Approximately 1×10^6 cells were harvested from either K562 or K562+ $\alpha_v \beta_3$ cell lines and resuspended into 1 mL of serum-free medium containing 10 μ M of the various decorated and undecorated block polypeptides. Cells were incubated at 37 °C for various times (20–240 min). After washing with HBSS thrice, 20 μ L of cell suspension was added to a 384-well plate with a #1.5 coverslip on the bottom. Cells were imaged on a Zeiss 710 inverted confocal (Oberkochen, Germany) equipped with a live cell chamber maintained at 37 °C using a 40× oil immersion objective.

Confocal Image Analysis. For analysis of the percentage of cells that show uptake of the polypeptides, the fluorescent channel and DIC channel were isolated and analyzed independently. In the fluorescent channel the lowest 10% of cell fluorescence was removed, to eliminate any autofluorescence from naïve K562 cells. Using this cutoff, locations and the area of green fluorescence were identified using the fluorescent channel only. The total number of cells was then counted using the DIC channel.

Alexa Fluorophore Labeling. The N-terminus and lysine residues in the RLP–ELP–Fn3 fusions were labeled with the NHS-ester derivative of Alexa488. To bias the reaction toward N-terminal labeling, the pH of the reaction mixture was adjusted to 8.3. The RLP–ELP diblock polypeptides, dissolved in 0.1 M sodium bicarbonate buffer (pH = 8.3), were incubated with a molar excess of dye (with a dye-to-protein molar ratio depending on the total number of reactive groups in the proteins, which includes lysine residues and the N-terminus (e.g., dye:RLP $_{20}$ = 2:1, dye:RLP $_{20}$ –Fn3 is 5:1), for 2 h at room temperature with continuous agitation. Excess dye was removed with 3 rounds of dialysis over 3 days at 4 °C with a 1:500 volume ratio of reaction mixture to milli-Q water. The samples were lyophilized and stored at -20 °C.

ASSOCIATED CONTENT

S Supporting Information

The Supporting Information is available free of charge on the ACS Publications website at DOI: 10.1021/acs.nanolett.9b02095.

ELP sequences, turbidimetry plots, dynamic light scattering plots, plots of refractive index, static light scattering partial Zimm plots, additional cryo-TEM images, and additional confocal images (PDF)

AUTHOR INFORMATION

Corresponding Author

*E-mail: chilkoti@duke.edu.

ORCID ®

Michael Dzuricky: 0000-0002-1775-2132 Ashutosh Chilkoti: 0000-0002-1569-2228

Author Contributions

M.D., X.S., and A.C. designed experiments. M.D., X.S., and P.W. performed the experiments and analyzed the data. M.D. and A.C. wrote the manuscript. All authors have given approval to the final version of the manuscript.

Funding

This work was supported by the NSF through NSF DMREF (DMR-17-29671), and the NIH through grant NIH MIRA

R35GM127042 to A.C. This work utilized facilities supported in part by the National Science Foundation under Agreement DMR-0944772.

Notes

The authors declare no competing financial interest.

ACKNOWLEDGMENTS

We acknowledge the Duke University Shared Materials and Instrumentation Facility for maintaining the cryo-TEM instrument used in this work.

REFERENCES

- (1) Xu, Z. P.; Zeng, Q. H.; Lu, G. Q.; Yu, A. B. Chem. Eng. Sci. 2006, 61 (3), 1027–1040.
- (2) Liong, M.; Lu, J.; Kovochich, M.; Xia, T.; Ruehm, S. G.; Nel, A. E.; Tamanoi, F.; Zink, J. I. ACS Nano 2008, 2 (5), 889–96.
- (3) Loh, X. J.; Lee, T. C.; Dou, Q.; Deen, G. R. *Biomater. Sci.* **2016**, 4 (1), 70–86.
- (4) Ehlerding, E. B.; Chen, F.; Cai, W. Adv. Sci. (Weinh) 2016, 3 (2), 1500223.
- (5) Wang, H.; Huang, Q.; Chang, H.; Xiao, J.; Cheng, Y. *Biomater. Sci.* **2016**, 4 (3), 375–90.
- (6) Kesharwani, P.; Jain, K.; Jain, N. K. Prog. Polym. Sci. 2014, 39 (2), 268-307.
- (7) Sharma, A. K.; Gothwal, A.; Kesharwani, P.; Alsaab, H.; Iyer, A. K.; Gupta, U. Drug Discovery Today 2017, 22 (2), 314–326.
- (8) Palmerston Mendes, L.; Pan, J.; Torchilin, V. P. *Molecules* **2017**, 22 (9), 1401.
- (9) Gillies, E.; Frechet, J. *Drug Discovery Today* **2005**, 10 (1), 35–43.
- (10) Sharma, S.; Parmar, A.; Kori, S.; Sandhir, R. *TrAC, Trends Anal. Chem.* **2016**, *80*, 30–40.
- (11) Swider, E.; Koshkina, O.; Tel, J.; Cruz, L. J.; de Vries, I. J. M.; Srinivas, M. Acta Biomater. 2018, 73, 38-51.
- (12) Astete, C. E.; Sabliov, C. M. J. Biomater. Sci., Polym. Ed. 2006, 17 (3), 247–289.
- (13) Lee, J. S.; Feijen, J. J. Controlled Release 2012, 161 (2), 473-83.
- (14) Meng, F.; Zhong, Z.; Feijen, J. Biomacromolecules 2009, 10 (2), 197–209.
- (15) LoPresti, C.; Lomas, H.; Massignani, M.; Smart, T.; Battaglia, G. J. Mater. Chem. **2009**, 19 (22), 3576.
- (16) Torchilin, V. P. Nat. Rev. Drug Discovery 2005, 4 (2), 145-60.
- (17) Malam, Y.; Loizidou, M.; Seifalian, A. M. Trends Pharmacol. Sci. 2009, 30 (11), 592-9.
- (18) Lukyanov, A. N.; Elbayoumi, T. A.; Chakilam, A. R.; Torchilin, V. P. *J. Controlled Release* **2004**, *100* (1), 135–44.
- (19) Chen, Z. G. Trends Mol. Med. 2010, 16 (12), 594-602.
- (20) Banerjee, D.; Sengupta, S. Prog. Mol. Biol. Transl Sci. 2011, 104, 489–507.
- (21) Steichen, S. D.; Caldorera-Moore, M.; Peppas, N. A. Eur. J. Pharm. Sci. 2013, 48 (3), 416–27.
- (22) Thakor, A. S.; Jokerst, J. V.; Ghanouni, P.; Campbell, J. L.; Mittra, E.; Gambhir, S. S. J. Nucl. Med. **2016**, 57 (12), 1833–1837.
- (23) Ni, D.; Bu, W.; Ehlerding, E. B.; Cai, W.; Shi, J. Chem. Soc. Rev. **2017**, 46 (23), 7438–7468.
- (24) Burke, B. P.; Cawthorne, C.; Archibald, S. J. Philos. Trans. R. Soc., A 2017, 375, 20170261.
- (25) Yousefpour, P.; McDaniel, J. R.; Prasad, V.; Ahn, L.; Li, X.; Subrahmanyan, R.; Weitzhandler, I.; Suter, S.; Chilkoti, A. *Nano Lett.* **2018**, *18*, 7784.
- (26) Jokerst, J. V.; Lobovkina, T.; Zare, R. N.; Gambhir, S. S. *Nanomedicine (London, U. K.)* **2011**, *6* (4), 715–28.
- (27) Suk, J. S.; Xu, Q.; Kim, N.; Hanes, J.; Ensign, L. M. Adv. Drug Delivery Rev. 2016, 99 (A), 28-51.
- (28) Maeda, H.; Matsumura, Y. Crit. Rev. Ther. Drug Carrier Syst. **1989**, 6 (3), 193–210.
- (29) Maeda, H. Adv. Enzyme Regul. 2001, 41 (1), 189-207.

(30) Albanese, A.; Tang, P. S.; Chan, W. C. Annu. Rev. Biomed. Eng. **2012**, *14*, 1–16.

- (31) Chithrani, B. D.; Chan, W. C. Nano Lett. 2007, 7 (6), 1542-1550.
- (32) Chithrani, B. D.; Ghazani, A. A.; Chan, W. C. Nano Lett. 2006, 6 (4), 662–668.
- (33) Kelly, J. Y.; DeSimone, J. M. J. Am. Chem. Soc. **2008**, 130 (16), 5438–9.
- (34) Napier, M. E.; DeSimone, J. M. Journal of Macromolecular Science, Part C: Polymer Reviews 2007, 47 (3), 321-327.
- (35) Petros, R. A.; DeSimone, J. M. Nat. Rev. Drug Discovery **2010**, 9 (8), 615–27.
- (36) Rolland, J. P.; Maynor, B. W.; Euliss, L. E.; Exner, A. E.; Denison, G. M.; DeSimone, J. M. *J. Am. Chem. Soc.* **2005**, *127* (28), 10096–100.
- (37) Champion, J. A.; Katare, Y. K.; Mitragotri, S. J. Controlled Release 2007, 121 (1-2), 3-9.
- (38) Champion, J. A.; Mitragotri, S. Pharm. Res. **2009**, 26 (1), 244–9.
- (39) Champion, J. A.; Walker, A.; Mitragotri, S. *Pharm. Res.* **2008**, *25* (8), 1815–21.
- (40) Mitragotri, S.; Lahann, J. Nat. Mater. 2009, 8 (1), 15-23.
- (41) Sharma, G.; Valenta, D. T.; Altman, Y.; Harvey, S.; Xie, H.; Mitragotri, S.; Smith, J. W. J. Controlled Release 2010, 147 (3), 408–412.
- (42) Venkataraman, S.; Hedrick, J. L.; Ong, Z. Y.; Yang, C.; Ee, P. L.; Hammond, P. T.; Yang, Y. Y. Adv. Drug Delivery Rev. 2011, 63 (14–15), 1228–46.
- (43) Truong, N. P.; Whittaker, M. R.; Mak, C. W.; Davis, T. P. Expert Opin. Drug Delivery 2015, 12 (1), 129-42.
- (44) Truong, N. P.; Quinn, J. F.; Whittaker, M. R.; Davis, T. P. Polym. Chem. 2016, 7 (26), 4295-4312.
- (45) Karagoz, B.; Esser, L.; Duong, H. T.; Basuki, J. S.; Boyer, C.; Davis, T. P. *Polym. Chem.* **2014**, *5* (2), 350–355.
- (46) Dalhaimer, P.; Bates, F. S.; Discher, D. E. Macromolecules 2003, 36 (18), 6873-6877.
- (47) Muro, S. J. Controlled Release 2012, 164 (2), 125-37.
- (48) Bae, Y. H.; Park, K. J. Controlled Release 2011, 153 (3), 198-205.
- (49) Rosenholm, J. M.; Sahlgren, C.; Linden, M. *Nanoscale* **2010**, 2 (10), 1870–83.
- (50) Elvin, C. M.; Carr, A. G.; Huson, M. G.; Maxwell, J. M.; Pearson, R. D.; Vuocolo, T.; Liyou, N. E.; Wong, D. C.; Merritt, D. J.; Dixon, N. E. *Nature* **2005**, *437* (7061), 999–1002.
- (51) Vrhovski, B.; Jensen, S.; Weiss, A. S. Eur. J. Biochem. 1997, 250 (1), 92-98.
- (52) Weitzhandler, I.; Dzuricky, M.; Hoffmann, I.; Garcia Quiroz, F.; Gradzielski, M.; Chilkoti, A. *Biomacromolecules* **2017**, 18 (8), 2419–2426
- (53) Niu, J. X.; Zhang, W. J.; Ye, L. Y.; Wu, L. Q.; Zhu, G. J.; Yang, Z. H.; Grau, G. E.; Lou, J. N. Eur. J. Cancer Prev. 2007, 16 (6), 517–27.
- (54) Weis, S. M.; Cheresh, D. A. Cold Spring Harbor Perspect. Med. **2011**, 1 (1), a006478.
- (55) Liu, Z.; Wang, F.; Chen, X. Drug Dev. Res. 2008, 69 (6), 329-339
- (56) Schnell, O.; Krebs, B.; Wagner, E.; Romagna, A.; Beer, A. J.; Grau, S. J.; Thon, N.; Goetz, C.; Kretzschmar, H. A.; Tonn, J. C.; Goldbrunner, R. H. *Brain Pathol.* **2008**, *18* (3), 378–86.
- (57) Wechsel, H.; Petri, E.; Feil, G.; Nelde, H.; Bichler, K.; Loesr, W. *Anticancer research* **1999**, 19 (2C), 1529–1532.
- (58) Carreiras, F.; Denoux, Y.; Staedel, C.; Lehmann, M.; Sichel, F.; Gauduchon, P. *Gynecol. Oncol.* **1996**, *62* (2), 260–7.
- (59) Zhao, Y.; Bachelier, R.; Treilleux, I.; Pujuguet, P.; Peyruchaud, O.; Baron, R.; Clement-Lacroix, P.; Clezardin, P. *Cancer Res.* **2007**, *67* (12), 5821–30.
- (60) Bowditch, R. D.; Hariharan, M.; Tominna, E. F.; Smith, J. W.; Yamada, K. M.; Getzoff, E. D.; Ginsberg, M. H. *J. Biol. Chem.* **1994**, 269 (14), 10856–10863.

(61) Richards, J.; Miller, M.; Abend, J.; Koide, A.; Koide, S.; Dewhurst, S. *J. Mol. Biol.* **2003**, 326 (5), 1475–1488.

- (62) Hassouneh, W.; Fischer, K.; MacEwan, S. R.; Branscheid, R.; Fu, C. L.; Liu, R.; Schmidt, M.; Chilkoti, A. *Biomacromolecules* **2012**, 13 (5), 1598–605.
- (63) Duan, J.; Wu, J.; Valencia, C. A.; Liu, R. Biochemistry **2007**, 46 (44), 12656-64.
- (64) McDaniel, J. R.; Mackay, J. A.; Quiroz, F. G.; Chilkoti, A. Biomacromolecules 2010, 11 (4), 944–52.
- (65) MacEwan, S. R.; Hassouneh, W.; Chilkoti, A. J. Visualized Exp. 2014, 88, e51583.
- (66) Parker, M. H.; Chen, Y.; Danehy, F.; Dufu, K.; Ekstrom, J.; Getmanova, E.; Gokemeijer, J.; Xu, L.; Lipovsek, D. *Protein Eng., Des. Sel.* 2005, 18 (9), 435–44.
- (67) Wilkins, D. K.; Grimshaw, S. B.; Receveur, V.; Dobson, C. M.; Jones, J. A.; Smith, L. J. *Biochemistry* **1999**, 38 (50), 16424–16431.
- (68) Wang, J.; Dzuricky, M.; Chilkoti, A. Nano Lett. 2017, 17 (10), 5995-6005.
- (69) McDaniel, J. R.; Weitzhandler, I.; Prevost, S.; Vargo, K. B.; Appavou, M. S.; Hammer, D. A.; Gradzielski, M.; Chilkoti, A. *Nano Lett.* **2014**, *14* (11), 6590–8.
- (70) Ortega, A.; García de la Torre, J. J. Chem. Phys. **2003**, 119 (18), 9914–9919.
- (71) McKenzie, M.; Ha, S. M.; Rammohan, A.; Radhakrishnan, R.; Ramakrishnan, N. *Biophys. J.* **2018**, *114* (8), 1830–1846.
- (72) Champion, J. A.; Mitragotri, S. Proc. Natl. Acad. Sci. U. S. A. **2006**, 103 (13), 4930-4.
- (73) Borst, A. J.; James, Z. M.; Zagotta, W. N.; Ginsberg, M.; Rey, F. A.; DiMaio, F.; Backovic, M.; Veesler, D. *Structure* **2017**, 25 (11), 1732–1739.
- (74) Graff, C. P.; Wittrup, K. D. Cancer research 2003, 63 (6), 1288-1296.
- (75) Jurney, P.; Agarwal, R.; Singh, V.; Choi, D.; Roy, K.; Sreenivasan, S. V.; Shi, L. J. Controlled Release 2017, 245, 170–176.
- (76) Xie, X.; Liao, J.; Shao, X.; Li, Q.; Lin, Y. Sci. Rep. 2017, 7 (1), 3827.
- (77) Mastria, E. M.; Chen, M.; McDaniel, J. R.; Li, X.; Hyun, J.; Dewhirst, M. W.; Chilkoti, A. J. Controlled Release 2015, 208, 52–8. (78) McDaniel, J. R.; Bhattacharyya, J.; Vargo, K. B.; Hassouneh, W.;
- (78) McDaniel, J. R.; Bhattacharyya, J.; Vargo, K. B.; Hassouneh, W.; Hammer, D. A.; Chilkoti, A. Angew. Chem., Int. Ed. 2013, 52 (6), 1683–7.
- (79) McDaniel, J. R.; MacEwan, S. R.; Li, X.; Radford, D. C.; Landon, C. D.; Dewhirst, M.; Chilkoti, A. *Nano Lett.* **2014**, *14* (5), 2890–5.
- (80) Mastria, E. M.; Cai, L. Y.; Kan, M. J.; Li, X.; Schaal, J. L.; Fiering, S.; Gunn, M. D.; Dewhirst, M. W.; Nair, S. K.; Chilkoti, A. J. Controlled Release 2018, 269, 364–373.
- (81) MacEwan, S. R.; Chilkoti, A. Nano Lett. 2014, 14 (4), 2058-64.
- (82) Hassouneh, W.; Zhulina, E. B.; Chilkoti, A.; Rubinstein, M. *Macromolecules* **2015**, 48 (12), 4183–4195.